Using CEST NMR to discover previously unobserved states on the free energy surface of proteins: Application to the L99A cavity mutant of T4 lysozyme

Received for publication, October 12, 2025, and in revised form, November 18, 2025 Published, Papers in Press, November 27, 2025
https://doi.org/10.1016/j.jbc.2025.110989

Ved Prakash Tiwari[1], Nihar Pradeep Khandave[1], D. Flemming Hansen[2,3], Guillaume Bouvignies[4], Lewis E. Kay[5,6,7,8,*], and Pramodh Vallurupalli[1,*]

From the [1]Tata Institute of Fundamental Research, Hyderabad, Telangana, India; [2]Department of Structural and Molecular Biology, Division of Biosciences, University College London, London, UK; [3]The Francis Crick Institute, London, UK; [4]Chimie Physique Chimie du Vivant (CPCV), Departement de chimie, Ecole normale superieure, PSL University, Sorbonne Universite, CNRS, Paris, France; [5]Department of Molecular Genetics, University of Toronto, Toronto, Ontario, Canada; [6]Department of Biochemistry, University of Toronto, Toronto, Ontario, Canada; [7]Department of Chemistry, University of Toronto, Toronto, Ontario, Canada; [8]Program in Molecular Medicine, Hospital for Sick Children Research Institute, Toronto, Ontario, Canada

Reviewed by members of the JBC Editorial Board. Edited by Wolfgang Peti

Carr-Purcell-Meiboom-Gill (CPMG) relaxation dispersion experiments establish that at room temperature, the L99A cavity mutant of T4 lysozyme (L99A T4L) interconverts between two compact folded conformations on the millisecond timescale. These include the native state in which the sidechain of Phe114 is exposed to solvent (E state) and a near-native minor state in which the aromatic moiety of Phe114 is buried in the core of the protein (B state, ∼2%). Molecular dynamics simulations that have captured the E to B interconversion in L99A T4L and related mutants suggest that these proteins adopt compact folded conformations other than E and B, yet extensive CPMG studies have not detected such states. In an effort to detect these more elusive conformers experimentally, we have recorded Chemical Exchange Saturation Transfer (CEST) experiments, as the widths of minor state dips in the resulting CEST profiles are sensitive to additional, even more sparse, conformers. Analysis of amide ^{15}N and $^{13}CH_3$ CEST profiles recorded on L99A T4L show that in addition to states E and B, a rare state (I) populated to ∼0.2% (11.5 °C) exchanges rapidly with state B. CEST-based urea *m*-values establish that all three states are compact, with interconversion between them proceeding *via* compact transition states. This study highlights the utility of CEST to characterize the free energy surface of a protein by detecting states with a wide range of lifetimes (100 ms to 100 μs) in ways that are not possible using other relaxation-based NMR techniques.

At physiological temperatures protein molecules transition between different conformational states, some of which play crucial roles in function, as well as in processes such as folding, misfolding, and aggregation (1, 2). Molecular function is, thus, predicated on the interplay between an array of diverse conformational states and how these interconvert with one another. The populations of such states are determined by their free energies, while the rates at which two states interconvert with each other depend on the height of the free energy barrier that separates them. Characterization of the free energy surfaces (FESs) of proteins is, therefore, an active field of research, involving a range of experimental and computational methods (2–8). NMR spectroscopy is a particularly powerful technique for the study of biomolecular conformational dynamics as it can be used to detect motions over the microsecond to second time-scale at almost every site in the molecule (2, 9–13). Often, the dynamics involve a dominant ground state that is populated to more than ∼90%, which exchanges with different minor conformational states. Due to their low populations and short lifetimes, these minor states are often not visible in regular NMR spectra (14). Consequently, experiments of the Carr-Purcell-Meiboom-Gill (CPMG) (15–17), $R_{1\rho}$ (18, 19), Chemical Exchange Saturation Transfer (CEST) (20–23), or Dark State Exchange Saturation Transfer (DEST) (9, 24) variety, that manipulate magnetization of the visible major state to detect invisible minor states, are used to study conformational exchange. A common feature of all these NMR experiments is the presence of a relaxation delay (T_{EX}) during which exchange occurs, with the exchange quantified through the application of radio-frequency pulses, either continuous or separated by delays, that modulate intensities or linewidths of magnetization from the visible state. The resulting datasets are then analyzed to characterize the underlying exchange process(es). Often chemical shift changes accompany the exchange between states, but this is not a prerequisite for some of the experiments, where minor states can be detected in the absence of such shift differences so long as the magnetization from the sites probed have significantly different transverse relaxation rates (R_2) in the minor and major conformations (9, 25, 26). Minor states populated typically to as low as ∼0.5% are detected in a variety of exchange processes in proteins (6, 27–32), nucleic acids (19, 33), and small molecules (34).

* For correspondence: Lewis E. Kay, lewis.kay@utoronto.ca; Pramodh Vallurupalli, pramodh@tifrh.res.in.

Over the last 3 decades the L99A cavity mutant of T4 lysozyme (L99A T4L) has emerged as a model system to study protein conformational dynamics (5, 35–40). The L99A mutation gives rise to an ∼150 Å^3 cavity buried in the C terminal domain of the protein, but it does not affect the structure of the native state of the molecule (41). In the lowest energy conformation (native state) of the protein, this cavity is buried with no direct path from the solvent reaching it. Nevertheless, hydrophobic molecules such as benzene can bind the cavity rapidly (37, 41) implying that the protein is dynamic, transiently adopting (higher energy) conformations in which there are pathways for the ligands from solvent to bind. The exact mechanism(s) by which this occurs continues to be investigated using various computational techniques (5, 42–44). CPMG-based relaxation dispersion studies carried out 2 decades ago to understand ligand binding in this system established the existence of an exchange process in the vicinity of the cavity, which turned out to be unrelated to the binding event. This process, which will be investigated further here, involves an interconversion between the native state and a minor conformer, the latter with a fractional population of ∼2.5% and a lifetime of ∼1.25 ms at 20 °C (36). The structure of the minor state was subsequently determined using CPMG-based data, showing that it is compact and folded, with a similar conformation to the native protein (38) (Fig. S1). The main differences in the structures are localized to the region around Phe114, where the backbone torsion angle ψ of this residue is changed from ∼ +55° in the native state to a helical value of ∼ −50° in the minor state. This change in dihedral angle results in the merging of helices f and g to form a long helix with a concomitant change in the orientation of the sidechain of Phe114 from a solvent exposed pose in the native state to one where the aromatic sidechain is inserted into the cavity in the minor state (Fig. S1). In what follows, therefore, the native state of L99A T4L is referred to as the exposed (E) conformer, as the sidechain of Phe114 is exposed to solvent, and the minor state is denoted as the buried (B) conformer, as the sidechain of Phe114 is within the cavity created by the L99A mutation. Notably, the B state cannot bind hydrophobic ligands as the cavity is occupied by the sidechain of Phe114. Since CPMG experiments could be interpreted to within experimental error on the basis of a simple, two-state E↔B interconversion, molecular dynamics studies were performed to obtain further insight into the E to B exchange process (5, 45–47). These computational studies suggested that the free energy surface of the protein is rugged, with the protein populating near native folded states other than B and E and that the E↔B interconversion occurs without any unfolding *via* both direct and indirect (*i.e.*, involving intermediates) pathways. There is, however, no direct experimental evidence supporting this level of ruggedness, as states other than B and E have not been observed at 25 °C or lower temperatures despite detailed investigations using CPMG-based NMR experiments over the last several years (16, 36, 38, 48–54).

CEST experiments can be used to study protein conformational exchange processes occurring on the ∼0.1 to ∼100 millisecond timescale (12, 55–58), and we showed recently that the widths of minor state dips in CEST profiles, arising from the slow interconversion between major and sparse conformations, can be used to inform on even more sparsely populated states that are in intermediate to fast exchange with the minor conformer (6, 8, 56, 59). That is, the minor state, that itself cannot be directly observed in regular NMR spectra and is detected *via* CEST, can be used to 'spy' on even more sparsely populated states. Here we have used this approach to investigate the E to B exchange process in L99A T4L using amide ^{15}N and methyl ^{13}C CEST experiments (11.5 °C). These experiments establish that L99A T4L populates a second minor state (I, ∼0.2% fractional population) that is in rapid exchange with B, providing experimental evidence of a more complex FES than previously established by CPMG studies, and consistent with MD simulations. Urea *m*-values of E, I, and B and the transition states connecting them, obtained through analysis of ^{15}N CEST data recorded on samples with varying concentrations of denaturant, indicate that state I is as compact as states E and B, and that interconversion between these conformers proceeds *via* compact transition states.

Results and discussion

CEST vs CPMG for exploring rugged protein energy landscapes

Both CEST and CPMG relaxation experiments are used to probe FESs of biomolecules, providing insights into functional dynamics that are not available from other biophysical techniques (2, 6, 8, 32, 60, 61). CPMG-based dispersion profiles of the L99A T4L cavity mutant were well fit to a two-state equilibrium involving the interconversion of folded states E and B (16, 36, 38, 48–54), as described in the Introduction, but further insight into the energy landscape of L99A T4L could not be obtained as additional states were not detected. Yet MD simulations showed a rugged FES, with multiple folded conformations. In an effort to obtain experimental support for states beyond E and B, we wondered whether CEST experiments might prove to be more useful than those based on CPMG relaxation dispersion. To address this possibility, initially computationally, we considered a linear three-state exchange process A↔B↔C involving a major state A, and two minor states, B and C, with p_A (97.25%) >> p_B (2.5%) >> p_C (0.25%) and exchange rates $k_{ex,AB}$ = 300 s^{-1} and $k_{ex,BC}$ = 5000 s^{-1}. Here p_i is the fractional population of state i and $k_{ex,ij} = k_{ij} + k_{ji}$ is the sum of the forward and reverse rates for the i↔j interconversion process. Synthetic CPMG data were generated for 58 combinations of $\Delta\varpi_{AB}$ and $\Delta\varpi_{AC}$ values (see legend to Fig. 1), where $\Delta\varpi_{ij} = \varpi_j - \varpi_i$ and ϖ_i and ϖ_j are the chemical shifts (ppm) of the spin in question in states i and j, respectively. The shift differences considered in this analysis are derived from experimental values obtained in a study of the folding of the A39G FF protein domain (6), and it has been assumed that the longitudinal (R_1) and transverse (R_2) relaxation rates of a given spin in each of the exchanging states are identical, $R_{1,A} = R_{1,B} = R_{1,C}$ = 1 s^{-1} and

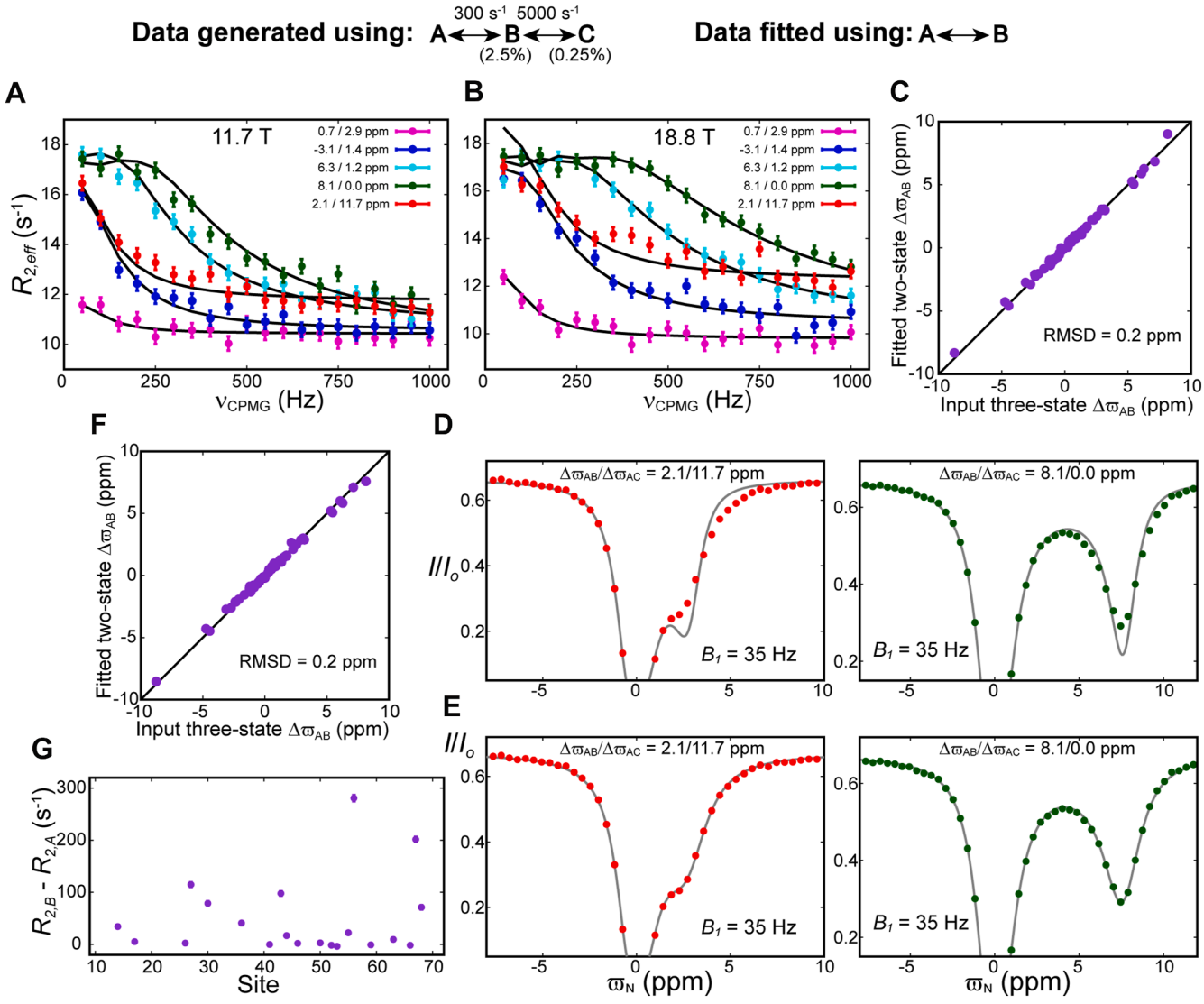

Figure 1. Minor states of interest that may go undetected in CPMG experiments can often be detected *via* CEST. *A* and *B*, calculated ^{15}N CPMG relaxation dispersion curves, B_0 = 11.7 T (*A*) and 18.8 T (*B*) and T_{EX} = 20 ms, for a three-state exchange process ($k_{ex,AB}$ = 300 s^{-1}, $k_{ex,BC}$ = 5000 s^{-1} and p_B = 2.5%, p_C = 0.25%) using different sets of $\Delta\varpi_{AB}$ and $\Delta\varpi_{AC}$ values. In *panels* (*A*) and (*B*) the synthetic CPMG data points are represented using colored circles, while the two-state best-fit to the data ($k_{ex,AB}$ = 292 ± 7 s^{-1} and p_B = 2.5 ± 0.1%, χ^2_{red} = 1) is shown using *black lines*. Chemical shift differences, $\Delta\varpi_{AB}$ and $\Delta\varpi_{AC}$, used to generate the synthetic CPMG profiles shown in (*A*) and (*B*) are listed in the *panels* as $\Delta\varpi_{AB}$/ $\Delta\varpi_{AC}$. Values of ($\Delta\varpi_{AB}$, $\Delta\varpi_{AC}$) were set to ($\Delta\varpi_{FI1}$, $\Delta\varpi_{FI2}$), obtained from fits of CEST profiles measured at 58 sites of the A39G FF domain (6) that folds from the unfolded to the native state (F) *via* intermediates I1 and I2. *C*, comparison of $\Delta\varpi_{AB}$ values used to generate the three-state exchange CPMG data with the corresponding $\Delta\varpi_{AB}$ shift differences from two-state fits of the resulting CPMG profiles. The signs of the CPMG derived (two-state) $\Delta\varpi_{AB}$ values were assumed to be the same as those used to generate the data. *D and E*, selected synthetic ^{15}N CEST profiles along with two-state fits; profiles were computed for B_1/T_{EX} = 17Hz/450 ms and 35Hz/400 ms, B_0 = 18.8 T, and generated using the same three-state exchange parameters used for the CPMG data. Fits carried out with (*D*) $R_{2,B} = R_{2,A}$ (χ^2_{red} = 2.2) and without (*E*) any constraint on $R_{2,B}$ ($k_{ex,AB}$ = 277 ± 2 s^{-1} and p_B = 2.8 ± 0.01%, χ^2_{red} = 1). The simulated data are shown using circles, while the grey lines are calculated using the best-fit parameters. The uncertainties in the I/I_0 values are smaller than the size of the filled circles. *F*, comparison between the $\Delta\varpi_{AB}$ values used to generate the CEST data for the three-state exchange process and those obtained from fits of a two-state exchange model to the data. *G*, very large best-fit $R_{2,B}$ values are obtained when a two-state model with $R_{2,B}$ unconstrained is fit to the synthetic three-state ^{15}N CEST data; ($R_{2,B}$ - $R_{2,A}$) values are only shown for sites for which $|\Delta\varpi_{AB}| > 2.0$ ppm.

$R_{2,A} = R_{2,B} = R_{2,C}$ = 10 s^{-1}. Five representative calculated ^{15}N CPMG relaxation dispersion profiles are shown in Figure 1*A* (11.7T/500 MHz) and 1*B* (18.8T/800 MHz) in which the effective transverse relaxation rates, $R_{2,eff}$, are denoted by filled circles. Interestingly, the synthetic CPMG datasets generated using the three-state exchange model can be fit (χ^2_{red} ~1.1) using a simple two state A↔B exchange process with $k_{ex,AB}$ = 292 ± 7 s^{-1} and p_B = 2.5 ± 0.1%. The two-state (A↔B) fits to the three state CPMG data were carried out by assuming $R_{2,A} = R_{2,B}$, and are shown with black lines in Figure 1, *A* and *B*. Visual inspection of all the fits shows that they are reasonable, and since χ^2_{red} ~1.1 there is no need to consider a more complicated exchange model to account for the data. Notably, the $\Delta\varpi_{AB}$ values obtained from the two-state fit are in very good agreement (RMSD 0.2 ppm, Fig. 1*C*) with the $\Delta\varpi_{AB}$ values used to generate the three-state data, further establishing that the CPMG experiment is very insensitive to the presence of state C, most likely due to its

low population and short lifetime. It is worth noting that in the example above, and in those following below, we fit two-state models of exchange (A↔B) to three-state exchange data (for example A↔B↔C). We do not mean to imply that A and B conformers in the two-state exchange model correspond to A and B, respectively, in the three-state model, although they often do, depending on exchange rates and populations. The extracted exchange parameters ($k_{ex,AB}$ = 292 s^{-1} and p_B = 2.5%) from the two-state fits of the simulated data are similar to those obtained from analysis of experimental data reporting on the L99A T4L E ↔ B interconversion process at ∼15 °C ($k_{ex,EB}$ ∼400 s^{-1} and p_B ∼2%) (36). Hence, states A and B in Figure 1 can be 'likened' to the E and B states of L99A T4L, respectively, while C corresponds to an additional minor state that cannot be detected by CPMG methods. The simulations of Figure 1, *A–C*, thus, rationalize why it has not been possible to observe conformers beyond E and B in our previous CPMG-based studies of L99A T4L.

Although CPMG experiments are typically preferred over their CEST counterparts for studies of μs – low ms exchange processes, it is now clear that CEST can be used to study dynamics over a wider timescale window (100 ms to 100 μs) than originally thought (100 ms to 5 ms). Indeed, in contrast to simulations of CPMG data discussed above where state C could not be detected, the situation is more favorable when one considers similar simulations of CEST profiles (6, 59). Synthetic CEST datasets (weak B_1 fields of 17 and 35 Hz; static magnetic field of 18.8T) were computed for an A↔B↔C exchange scheme, using the same exchange parameters and combinations of $\Delta\varpi_{AB}$ and $\Delta\varpi_{AC}$ values that were used to generate the CPMG data above. The resulting CEST profiles were then fit to a two-state A↔B exchange model and the data were only poorly reproduced when the condition $R_{2,A} = R_{2,B}$ was enforced (χ^2_{red} = 2.2), Figure 1*D*. However, the quality of the fits was much better (χ^2_{red} = 1) when an A↔B exchange model was used in which both $R_{2,A}$ and $R_{2,B}$ were independent fitting parameters, with best fit values of $k_{ex,AB}$ = 277 ± 2 s^{-1} and p_B = 2.8 ± 0.01% (Fig. 1*E*). The fitted two-state $\Delta\varpi_{AB}$ values are once again in good agreement (RMSD 0.2 ppm) with those used to generate the data (Fig. 1*F*), but $R_{2,B}$ values are significantly elevated, with some larger than 75 s^{-1} compared to $R_{2,B}$ = 10 s^{-1} used to generate the profiles (Fig. 1*G*). It is noteworthy that, as in the analysis of the synthetic CPMG data, fitted chemical shift values from CEST datasets that appear consistent with expectations (in the present case 'correct' $\Delta\varpi_{AB}$ values were obtained from fits to the 'incorrect' two-state model) cannot be used as an argument for the legitimacy of an assumed kinetic scheme. Rather, the elevated extracted transverse relaxation rates in Figure 1*G* are a telltale sign of a more complex exchange mechanism than that assumed, whereby the dips derived from state B are broadened due to exchange with an additional sparse state C (6, 20, 59, 62). In the analysis of experimental data, it is, in general, relatively straightforward to establish that the extracted relaxation rates (which in principle should be intrinsic relaxation values) are larger than expected, and hence reporting on a more complex exchange scheme than that used in fits, since R_2 values can be estimated from the size of the complex studied (6, 20, 59, 62). Thus, CEST profiles can provide information on multi-state exchange processes even when only a single minor exchange dip is observed and when such information is not available from the analysis of CPMG data. However, one must exercise caution while applying the above strategy to coupled spins, as in the case of ^{13}C CEST data recorded on uniformly ^{13}C labeled samples or ^{1}H CEST data because the shapes of the resulting CEST profiles are affected by J_{CC} couplings or ^{1}H–^{1}H dipolar interactions respectively.

Application of CEST to study of the FES of L99A T4L

Having established that it may be possible to detect additional states from analysis of CEST data that have eluded observation when using CPMG experiments we next recorded amide ^{15}N and methyl ^{13}C CEST datasets using a [U-^{15}N; ^{2}H; Ileδ1-$^{13}CH_3$; Leu, Val-$^{13}CH_3/^{12}CD_3$] labeled L99A T4L sample at 11.5 °C (Fig. 2, *A–J*; 16.4 T). Several CEST profiles showed a dip corresponding to a minor state (Fig. 2, *C–J*) in addition to one derived from the major conformer, but the ^{15}N (B_1 = 18.1, 33.2, 51.8, 72.6, and 129.6 Hz; B_0 = 16.4 T) and $^{13}CH_3$ (B_1 = 16.2, 32.4, 49.1, and 98.2 Hz, B_0 = 16.4 T) data could not be jointly fit to a two-state exchange model in which the major and minor state R_2 values were constrained to be the same (χ^2_{red} = 2.2, Fig. 2, *C–F*). However, a two-state exchange model with no constraint on major and minor state R_2 values fit the CEST data better (χ^2_{red} = 1.2, Fig. 2, *G–J*), albeit with large $R_{2,B}$ values at some sites (Fig. 2*K*). Extracted $\Delta\varpi$ values from these fits are in good agreement with those derived from analysis of CPMG dispersion profiles (RMSD 0.3 ppm, Fig. 2*L*), confirming that the CEST experiments probe the E↔B exchange process as well, with best-fit exchange parameters, $k_{ex,EB}$ = 294 ± 4 s^{-1} and p_B = 1.70 ± 0.01%. Importantly the elevated $R_{2,B}$ values (Fig. 2*K*) clearly establish the presence of at least one hitherto undiscovered minor state in exchange with state B. These $R_{2,B}$ values localize around the cavity (Fig. 2*M*), suggesting that residues in this region can adopt conformations other than those associated with the E and B states.

Next, we proceeded to test whether the addition of a single intermediate state, I, to the exchange scheme could account for the increased $R_{2,B}$ rates obtained *via* two-state analyses. The ^{15}N (B_1 = 18.1, 33.2, 51.8, 72.6 & 129.6 Hz; B_0 = 16.4 T) and methyl ^{13}C (B_1 = 16.2, 32.4, 49.1 & 98.2 Hz, B_0 = 16.4 T) CEST data were fit to a global triangular three-state exchange model in which E, B, and I exchange with each other subject to the constraint $R_{2,E} = R_{2,B} = R_{2,I}$. In the absence of any information regarding the minor-state chemical shifts, determining the right three-state exchange model from NMR relaxation dispersion data is challenging, often requiring extensive computation (60). However, recently we noted that the correct three-state model can be readily obtained so long as the signs of the chemical shift differences between the minor state resonances (*i.e.* signs of $\Delta\varpi_{BI}$ values here) are known (59). This information is captured in a two-state

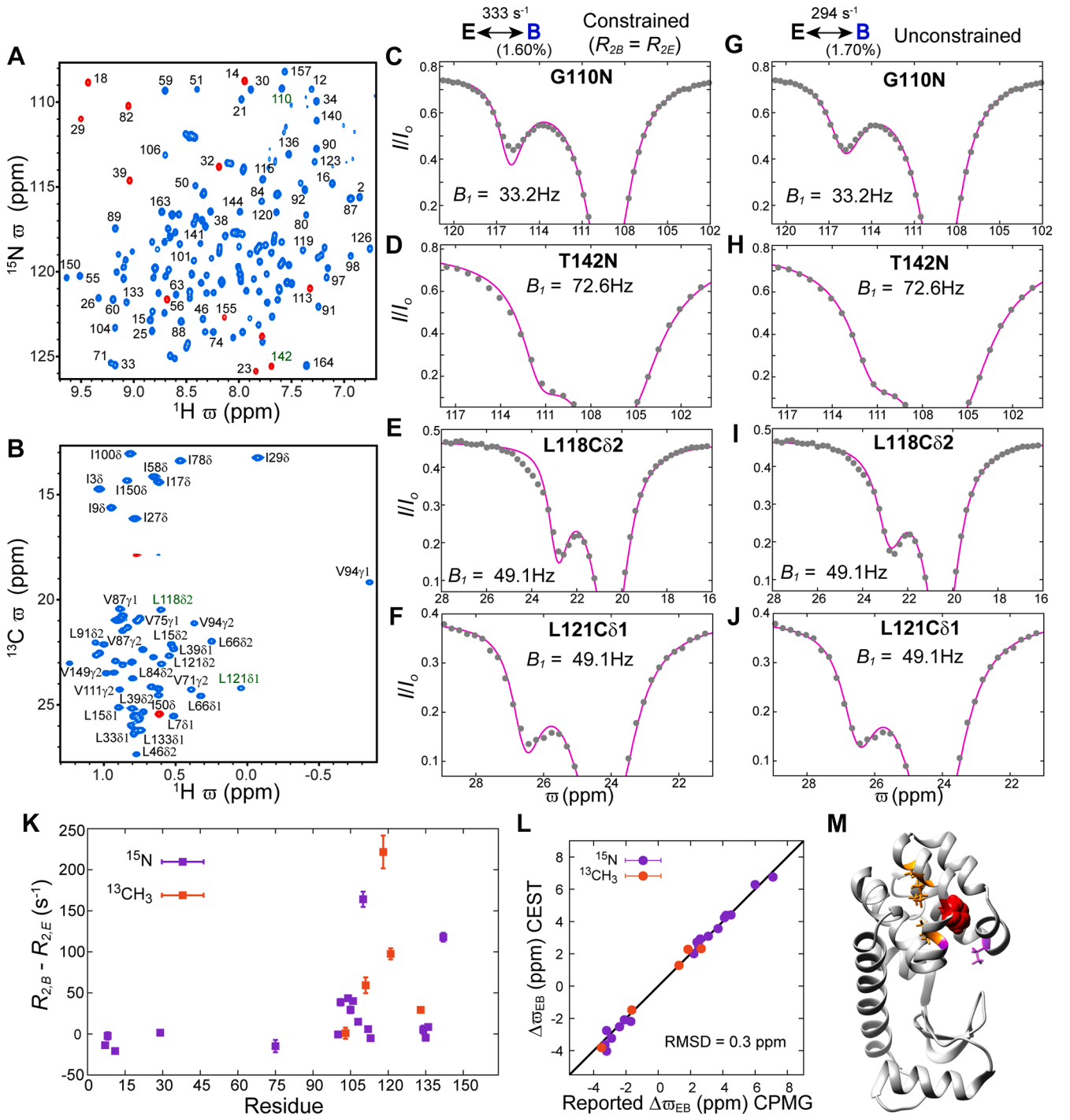

Figure 2. The 'invisible' B state of L99A T4L interconverts with even more sparsely populated state(s). Amide ^{1}H-^{15}N (*A*) and ILV methyl ^{1}H-^{13}C (*B*) HSQC spectra of L99A T4L (11.5 °C; 16.4 T). Only peaks from the major (E) state are visible in the spectra and (some well resolved peaks) are labelled according to the amide or methyl site from which they arise. Aliased peaks are shown in *red*. (*C–J*) Representative amide ^{15}N CEST profiles from G110 (*C*, *G*) and T142 (*D*, *H*), along with methyl ^{13}C CEST profiles from L118Cδ2 (*E*, *I*) and L121Cδ1 (*F*, *J*). Correlations arising from G110/T142 and L118Cδ2/L121Cδ1 are indicated in *green* in (*A*) and (*B*), respectively. A two-state (E↔B) model does not account for the CEST data when $R_{2,B} = R_{2,E}$ (*C–F*), however, noticeably better fits are obtained when $R_{2,B}$ is not constrained (*G–J*). The experimental data points are shown using *grey circles*, while the *magenta lines* are calculated using the best-fit parameters. The uncertainties in the I/I_0 values are smaller than the size of the filled circles. *K*, amide ^{15}N and methyl ^{13}C $R_{2,B}$ - $R_{2,E}$ values obtained from two-state fits where $R_{2,B}$ is not constrained; only values for amide ^{15}N sites with $|\Delta\varpi_{EB}| > 2.0$ ppm and for methyl ^{13}C sites with $|\Delta\varpi_{EB}| > 1.0$ ppm are shown. *L*, comparison of $\Delta\varpi_{EB}$ values obtained from the two-state analysis of the amide ^{15}N and methyl ^{13}CH$_3$ CEST data with corresponding shift differences obtained previously *via* analysis of CPMG-based datasets (38, 54). Signs for the CPMG-derived methyl ^{13}C $\Delta\varpi_{EB}$ values are not available and were assumed to be the same as those derived from the CEST experiments. *M*, ribbon representation of L99A T4L [PDB ID: 3DMV, (83)] showing residues with large (>50 s^{-1}) amide ^{15}N (*purple*) or methyl ^{13}CH$_3$ (*orange*) $R_{2,B}$ - $R_{2,E}$ values (stick representation). Phe114 is shown in *red* (CPK representation).

analysis of (low B_1) CEST data recorded at multiple temperatures (See Supporting Information, Fig. S2), and once available the correct three-state exchange model is obtained without extensive computation by constraining the signs of the chemical shift differences between the minor state resonances (here $\Delta\varpi_{BI} \geq 0$ for positive $\Delta\varpi_{BI}$ or $\Delta\varpi_{BI} \leq 0$ for negative $\Delta\varpi_{BI}$) during data fitting (59). In the case of L99A T4L, the three-state model obtained using this procedure fit the amide ^{15}N and methyl ^{13}C CEST data well, and slightly better than any of the two-state models attempted previously (compare Figure 3, *A* and *B* with Fig. 2, *C–J*). Exchange parameters $k_{ex,EB}$ = 297 ± 6 s^{-1}, $k_{ex,EI}$ = 170 ± 37 s^{-1}, $k_{ex,BI}$ = 1667 ± 44 s^{-1}, p_B = 1.5 ± 0.01%, and p_I = 0.22 ± 0.01% (χ^2_{red} = 1) were obtained, establishing that the conformational dynamics of L99A T4L can be well-modeled as a three-state exchange process involving states E, B, and a single new minor state (I). As expected, based on the simulations of Figure 1, the $\Delta\varpi_{EB}$ values derived from the CEST fits involving the three-state model are in good agreement with the corresponding shift differences obtained previously from two-state fits of CPMG data (16, 38) (RMSD 0.4 ppm, Fig. 3*C*). Moreover, the I state chemicals shifts (Table S4) differ from those of the B state (Fig. 3*D*) accounting for the broadening of the minor-state (B) dips in the CEST profiles. In addition to the triangular model, we also checked whether any of the simpler linear three-state models could explain the

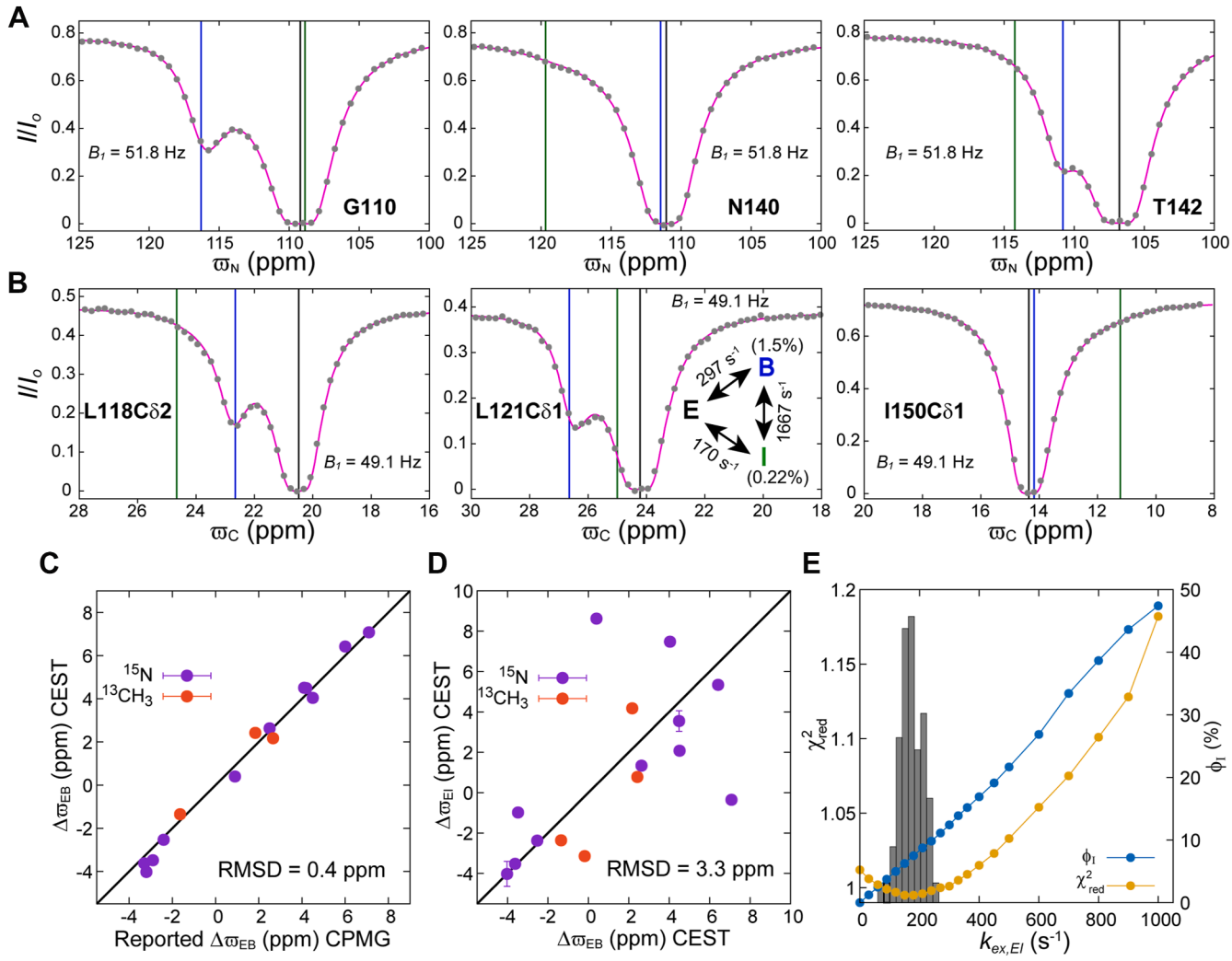

Figure 3. A three-state exchange model accounts for the L99A T4L CEST data (11.5 °C; 16.4 T). Fits of the amide ^{15}N CEST profiles (*A*) from G110, N140 and T142 and methyl ^{13}C (*B*) CEST profiles from L118Cδ2, L121Cδ1, and I150Cδ1 to a triangular model of chemical exchange (inset in the middle panel in (*B*)). *Grey circles* represent experimental data, while the *magenta line* is calculated from the best-fit (three-state) parameters. The uncertainties in the I/I_0 values are smaller than the size of the filled circles. *Black*, *blue*, and *green vertical lines* are drawn at the best-fit values of ϖ_E, ϖ_B, and ϖ_I, respectively. *C*, comparison of $\Delta\varpi_{EB}$ values obtained from the three-state analysis of amide ^{15}N and methyl ^{13}C CEST data with the corresponding shift differences from analysis of CPMG profiles (38, 54). Signs of the CPMG derived $\Delta\varpi_{EB}$ values for the methyl ^{13}C sites are not available and are assumed to be the same as those obtained from the CEST experiments. *D*, the poor correlation between $\Delta\varpi_{EI}$ and $\Delta\varpi_{EB}$ values obtained from the joint three-state analysis of the amide ^{15}N and methyl ^{13}C CEST profiles establish that states I and B are unique. *E*) χ^2_{red} *vs* $k_{ex,EI}$ (*yellow*), along with the distribution of fitted $k_{ex,EI}$ values from the three-state triangular model (*grey*), based on a joint analysis of the ^{15}N and ^{13}C CEST data. For each value of $k_{ex,EI}$ the fraction of molecules that convert from E to B *via* I ($\Phi_I = \left(k_{EI}\frac{k_{IB}}{k_{IE}+k_{IB}}\right) / \left(k_{EB}+k_{EI}\frac{k_{IB}}{k_{IE}+k_{IB}}\right)$) is also shown (*dark blue*). The distribution of fitted $k_{ex,EI}$ values was obtained *via* a bootstrap procedure (81, 82) with 100 trials.

CEST data, requiring that $R_{2,E} = R_{2,B} = R_{2,I}$ in all cases. The bifurcated I↔E↔B model, where I and B exchange independently with the major state E, did not fit the data well (χ^2_{red} ∼1.9) as it cannot account for the broadening of the B state dips in the CEST profiles. The linear E↔B↔I model where I is off-pathway does fit the data well (χ^2_{red} = 1.01) (Fig. S3), suggesting that the role of state I in the E↔B interconversion processes is likely small. This is consistent with the shallow minimum that is obtained in the χ^2_{red} *vs* $k_{ex,EI}$ surface for the triangular model (Fig. 3*E*), with a minimum $k_{ex,EI}$ value of ∼200 s^{-1}, but where $k_{ex,EI}$ can be quadrupled or quartered with little change in the goodness of fit. Figure 3*E* also plots the fraction of state B that is formed from state E along the E↔I↔B pathway of the triangular model, Φ_I (see legend to Fig. 3). Over the range of best-fit $k_{ex,EI}$ values ($\chi^2_{red} \leq 1.05$) $\Phi_I < 20\%$, consistent with a relatively small contribution from the I state in the conversion from E to B. As the CEST data indicate (Fig. 3*E*) that the direct (E to B) pathway dominates the interconversion between E and B, it is not surprising that the E↔I↔B linear on-pathway scheme, where the interconversion between E and B proceeds solely *via* I, does not account for the data (χ^2_{red} = 1.3) as well as the triangular and the linear E↔B↔I models (χ^2_{red} ∼1 in both cases). As mentioned in the introduction, MD simulations suggest that the E↔B interconversion proceeds both directly and indirectly *via* intermediates (5, 46). Thus, we prefer the triangular scheme over the E↔B↔I scheme as it supports the notion of both direct and indirect interconversion pathways from E to B (5, 46, 47), as observed in MD simulations (5, 46), with the direct E↔B transition being dominant. It should be noted that both the triangular and the linear E↔B↔I scheme result in very similar chi-squared statistics, minor state populations and chemical shifts (Fig. S3).

TFE (2,2,2-Trifluoroethanol) has previously been shown to stabilize certain sparsely populated states including some folding intermediates (63) and it has been used to increase the population of minor states in CEST NMR studies (6). Hence to test if the best-fit ϖ_I values are reasonable we added a small fraction of TFE to the sample with the hope of changing the relative populations of the B and I states so as to modify the shapes of the resulting CEST profiles in predictable ways that are consistent with the fitted chemical shifts. Addition of 8% TFE increased $k_{ex,BI}$ to ∼4000 s^{-1} and, more importantly, increased p_B and p_I to ∼2.2% and ∼1.8%, respectively, relative to values of 1.5 ± 0.01% (p_B) and 0.22 ± 0.01% (p_I) in the absence of the additive. ^{15}N CEST profiles in the absence and presence of TFE are compared in Figure 4, *A* and *B*, respectively. For G110, where $\varpi_I \sim \varpi_E$, the distinct dip at $\sim \varpi_B$ in the absence of TFE broadens significantly when TFE is added and shifts in-between ϖ_I and ϖ_B, as expected. In the case of N140, where $\varpi_B \sim \varpi_E$ so that a minor state dip is not visible in the $B_1 = 18.1$ Hz CEST profile in the absence of TFE, a broad dip emerges between ϖ_I and ϖ_B in the presence of TFE. In the case of T142 where ϖ_B, ϖ_E, and ϖ_I are all distinct, the minor state dip at $\sim \varpi_B$ in the absence of TFE broadens and shifts to a position between ϖ_B and ϖ_I when TFE is added. The shifts, broadening, and appearance of dips in these examples are consistent with expectations based on the assignments of chemical shifts in the absence of TFE. Further validation of the obtained chemical shifts is obtained by noting that the fitted ϖ_B and ϖ_I values generated from samples with and without TFE are similar (Fig. 4, *C* and *D*). Finally, ^{15}N CEST profiles calculated using ϖ_E, ϖ_B, and ϖ_I values from fits of datasets recorded on samples without TFE, but with exchange rates and populations obtained from fits of the TFE-based data (Fig. 4*E*), are qualitatively similar to the ^{15}N CEST profiles recorded on samples with TFE (Fig. 4*B*). Taken together, these results establish that the obtained ϖ_I values are robust.

With a three-state model of exchange for L99A T4L (11.5 °C) available from fits of CEST data (Fig. 3), it is now possible to understand why additional states beyond E and B could not be observed in CPMG experiments: the low population of state I and its rapid interconversion with state B effectively 'subsumes' state I into state B. We have simulated amide ^{15}N and methyl ^{13}C CPMG dispersion profiles (T_{EX} = 20 ms, with ν_{CPMG} varying from 50 to 1000 Hz) at fields of 11.7 T and 18.8 T using CEST parameters (triangular model) obtained from fits of 11 ^{15}N and 4 ^{13}C sites (Fig. S4). The synthetic CPMG profiles obtained were well fit with a two-state model of conformational exchange that assumed equivalent intrinsic transverse relaxation rates for corresponding spins in each state (χ^2_{red} = 1.04; $k_{ex,EB}$ = 318 ± 45 s^{-1} and p_B = 1.5 ± 0.3%).

We wondered whether the level of compactness of state, I is similar to states E and B, or whether I is more expanded, as might be expected in the case of a partially folded folding-intermediate (8, 64). It is not possible to address this question from amide ^{15}N and methyl ^{13}C chemical shifts alone. However, urea *m*-values (1, 65), that provide a measure of how the free energy (G) of a state changes with respect to a reference state, can be interpreted in terms of the compactness of the queried state, since expanded conformers, such as the unfolded ensemble of a protein, have a large number of urea binding sites leading to a high *m*-value. Here we define $m_K = -\frac{d\Delta G_{EK}}{d[urea]}$, where E is the reference ground state of L99A T4L, and K denotes either states I or B, or a transition state, TS_{LN}, that connects states L and N in which case m_{TSLN} is the *m*-value of TS_{LN}. Urea *m*-values for states B, I and all possible transition states were obtained by analyzing ^{15}N CEST data recorded using L99A T4L samples prepared with varying amounts of urea, 11.5 °C (Figs. 5, S5, Table S5). As expected from the structures of the E and B states, that are both well-folded (38, 41), m_B (=−0.4 ± 0.1 kJ mol^{-1} M^{-1}) ∼ 0. Similarly, m_I (=0.4 ± 0.1 kJ mol^{-1} M^{-1}) ∼ 0, so that the level of compactness of state I is similar to states E and B. The *m*-values of the transition-states are also small. For example, m_{TSEB} (=0.4 ± 0.2 kJ mol^{-1} M^{-1}) ∼ 0, consistent with interconversion between E and B without expansion of the protein, in agreement with MD simulations (5, 46). Interconversion between states B and I proceeds *via* a slightly expanded transition-state (m_{TSBI} = 1.2 ± 0.2 kJ mol^{-1} M^{-1}). However,

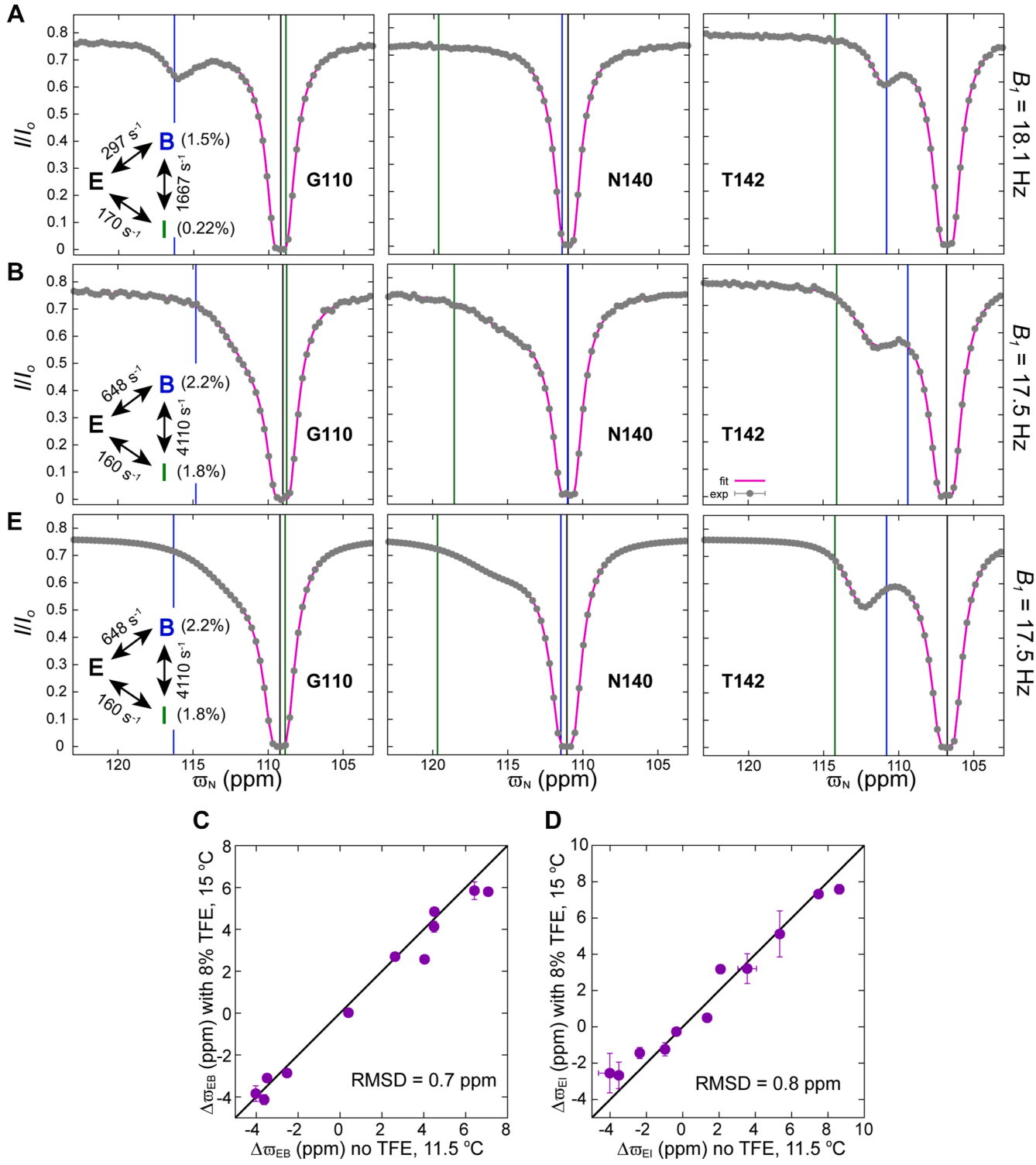

Figure 4. ϖ_I values obtained from the three-state analysis of the CEST data are robust. Amide ^{15}N CEST profiles from G110, N140 and T142 measured using samples without (*A*) or in the presence of TFE (8% V/V) (*B*). The CEST data shown in (*A*) and (*B*) are recorded at 11.5 °C and 15 °C, respectively. In (*A*) and (*B*), the best-fit three-state models are shown, along with *black, blue*, and *green vertical lines* drawn at the positions of the best-fit ϖ_E, ϖ_B, and ϖ_I values, respectively, obtained from the analysis of CEST data recorded in the absence (*A*) and presence (*B*) of TFE. The experimental data are represented using *grey circles*, with the *magenta lines* calculated using the (three-state) best-fit parameters. The uncertainties in the I/I_0 values are smaller than the size of the filled circles. Comparison of amide ^{15}N $\Delta\varpi_{EB}$ (*C*) and $\Delta\varpi_{EI}$ (*D*) values obtained from the analysis of the CEST data recorded with and without TFE. *E*, ^{15}N CEST profiles calculated using the chemical shifts from (*A*) and the exchange parameters indicated in the inset of the *left panel* in (*B*), obtained from fits of the 'TFE data', are qualitatively similar to the experimental CEST profiles in (*B*). In (*E*) *black, blue*, and *green vertical lines* are drawn at the positions of the best-fit ϖ_E, ϖ_B, and ϖ_I values, respectively, obtained in the absence of TFE (*A*).

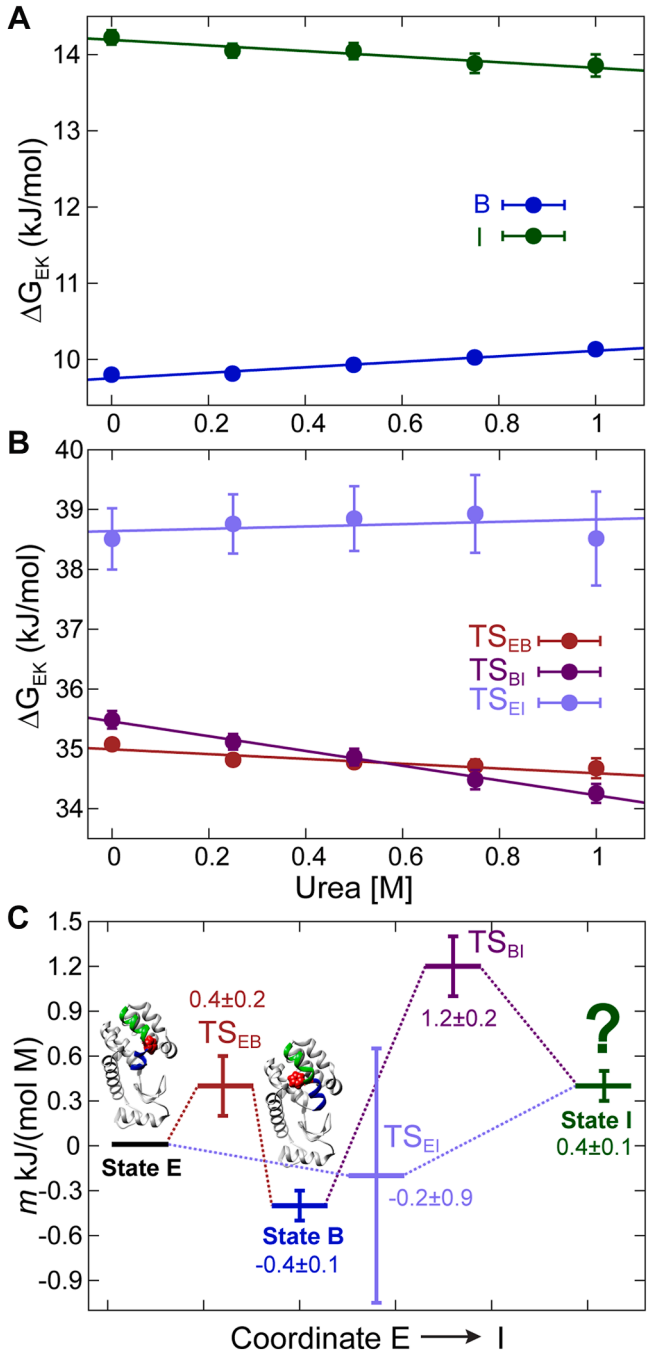

Figure 5. The FES of L99A T4L in the vicinity of the cavity consists of compact conformations. *A*, the change in free energy of states B and I (with respect to E) as function of urea concentration. For a state K, ΔG_{EK} is calculated from the populations according to the relation $\Delta G_{EK} = -RTln(p_K/p_E)$. *B*, changes in the free-energies of the transition states TS_{EB}, TS_{BI}, and TS_{EI} as a function of urea concentration. For TS_{LM}, ΔG_{ETSLM} is calculated from rates and populations using the relation $\Delta G_{ETSLM} = -RTln(p_L/p_E) - RTln(k_{LM}/C)$ where C is set to be 10^7 s^{-1} and does not affect the calculated m_{TSLM} value. *C*, schematic representation of the urea *m*-value landscape of L99A T4L, 11.5 °C. Structures of L99A T4L in the E [PDB: 3DMV (83)] and B [PDB: 2LCB (38)] states are also shown.

TS_{BI} is likely quite compact, as well. For example, a folding intermediate of the FF domain involving a relatively small structural change (66) where only five helix residues become disordered (relative to the folded state) has an *m*-value of ~3 kJ mol^{-1} M^{-1} (6). Finally, m_{TSEI}, though poorly defined, is also small (−0.2 ± 0.9 kJ mol^{-1} M^{-1}). Thus, the interconversion between the three compact states, E, B and I, proceeds *via* compact transition states.

Conclusion

CPMG relaxation dispersion experiments have traditionally been used to study µs-ms timescale conformational exchange processes in proteins, enabling quantitative measures of the kinetics and thermodynamics of interconversion, and structural information about the molecular players involved (15, 58, 67). Here, we demonstrate the utility of CEST-based relaxation experiments, which, at least for the case of the L99A cavity mutant of T4 lysozyme, provide deeper insights into exchange processes than the CPMG approach. Unlike CPMG profiles of L99A T4L that are well-fit to a two-state model of chemical exchange, CEST data unequivocally establish a third exchanging conformer, providing the first experimental evidence in support of MD simulations (5, 45–47) that the FES of this protein is rugged in a region around the cavity. Further insight is likely to be obtained by performing additional relaxation experiments on suitable mutants, as has been done in studies elucidating the folding mechanisms of proteins (6, 8, 64, 68, 69). The L99A T4L system provides an example of how combined NMR and computational approaches can be used to obtain an in-depth understanding of protein dynamics, with CEST experiments playing a prominent role in quantifying rates and populations of a limited number of states and serving to validate results from simulations, which can then be used with confidence to map out further atomistic details of the process under investigation.

Experimental procedures

NMR samples

L99A T4L was expressed in *E coli* BL21(DE3) cells grown in M9 media supplemented with the appropriate precursors (70) and purified as described previously (51). The protein sample used for most of the studies contained ~1.2 mM [U-^{15}N; ^{2}H; Ileδ1-$^{13}CH_3$; Leu, Val-$^{13}CH_3/^{12}CD_3$] (ILV) L99A T4L dissolved in 50 mM sodium phosphate, 25 mM NaCl, 2 mM NaN_3, 2 mM EDTA, pH 5.5, (10% D_2O) buffer. Samples used to validate the exchange model or to obtain urea *m*-values comprised ~1.5 mM of [U-^{15}N] L99A T4L dissolved in the above buffer but with either 8% V/V 2,2,2-trifluoroethanol (TFE) or the appropriate amount of urea (*m*-values).

NMR experiments

All amide ^{15}N CEST (20) and methyl ^{13}C CEST (71, 72) experiments were carried out on a Bruker 700 MHz Avance III HD spectrometer equipped with a triple resonance cryogenically cooled probe. Details are provided in the Supporting information (Tables S1–S3). The strengths of the ^{15}N or ^{13}C B_1 fields applied in the T_{EX} periods during which exchange is quantified were calibrated using the nutation method (73).

Generation of synthetic CPMG and CEST data

Synthetic ^{15}N and ^{13}C CPMG profiles were generated at static magnetic field (B_0) strengths of 11.7 T and 18.8 T by propagating the spin half Bloch-McConnell equations (74) for a sequence of π pulses in the context of the constant-time CW-CPMG experiment (16, 75, 76). Similarly, synthetic CEST data were generated at B_0 strengths of 18.8 T by propagating the Bloch-McConnell (74) equations for a T_{EX} period in the presence of weak B_1 irradiation. Details can be found in the Supporting Information.

Data analysis

NMR data were processed using the *NMRPipe* program (77), spectra were visualized and labeled using *Sparky* (78, 79), and, subsequently, peak intensities were extracted from pseudo-3D datasets using the program *PINT* (80). The software package *ChemEx* (https://github.com/gbouvignies/chemex) that numerically integrates the Bloch-McConnell equations (74) was used to fit various exchange models to the CEST and CPMG data and to extract the best-fit exchange parameters. Two (6, 20) and three-state (59) analyses of the CEST datasets were carried out as described previously, with details in the Supporting Information. Uncertainties in the fitted parameters were estimated using either bootstrap or Monte-Carlo approaches (81, 82), as described previously (59).

Data availability

The CEST datasets analyzed during the current study are available from the corresponding authors upon reasonable request.

Supporting information—The supporting information available free of charge from the journal website consists of a pdf file that contains additional experimental details, Supplementary figures and parameters (exchange rates, populations and chemical shifts) from the analysis of the CEST data (84).

Acknowledgment—PV thanks the TIFRH NMR facility for spectrometer time and Dr Krishna Rao for maintaining the facility.

Author contributions—P. V., L. E. K., G. B., D. F. H., N. P. K., and V. P. T. conceptualization.

Funding and additional information—This work was funded by intramural funds from TIFR Hyderabad (DAE, Government of India, Project No. RTI 4007) to PV. DFH was supported by the UKRI and EPSRC (DFH; EP/X,036,782/1). LEK. acknowledges support from the Canadian Institutes of Health Research (CIHR) (FND-503573) and the Natural Sciences and Engineering Council of Canada (024–03872). GB acknowledges support from the Agence Nationale de la Recherche (ANR-24-CE29–6543). For the purpose of open access, the authors have applied a Creative Commons Attribution (CC BY) licence to any Author Accepted Manuscript version arising.

Conflict of interest—The authors declare that they do not have any conflicts of interest with the content of this article.

Abbreviations—The abbreviations used are: CEST, Chemical Exchange Saturation Transfer; CPMG, Carr-Purcell-Meiboom-Gill; FES, Free Energy Surface; NMR, Nuclear Magnetic Resonance; T4L, T4 Lysozyme; TFE, 2,2,2-Trifluoroethanol.

References

1. Bahar, I., Jernigan, R., and Dill, K. A. (2017) *Protein Actions: Principles and Modeling, Garland Science*, Taylor & Francis Group, New York
2. Sekhar, A., and Kay, L. E. (2019) An NMR view of protein dynamics in health and disease. *Annu. Rev. Biophys.* **48**, 297–319
3. Eaton, W. A. (2021) Modern kinetics and mechanism of protein folding: a retrospective. *J. Phys. Chem. B* **125**, 3452–3467
4. Aviram, H. Y., Pirchi, M., Barak, Y., Riven, I., and Haran, G. (2018) Two states or not two states: single-molecule folding studies of protein L. *J. Chem. Phys.* **148**, 123303
5. Wang, Y., Papaleo, E., and Lindorff-Larsen, K. (2016) Mapping transiently formed and sparsely populated conformations on a complex energy landscape. *Elife* **5**, e17505
6. Tiwari, V. P., Toyama, Y., De, D., Kay, L. E., and Vallurupalli, P. (2021) The A39G FF domain folds on a volcano-shaped free energy surface via separate pathways. *Proc. Natl. Acad. Sci. U.S.A.* **118**, e2115113118
7. Vallurupalli, P., Tiwari, V. P., and Ghosh, S. (2019) A double-resonance CEST experiment to study multistate protein conformational exchange: an application to protein folding. *J. Phys. Chem. Lett.* **10**, 3051–3056
8. De, D., Thapliyal, N., Prakash Tiwari, V., Toyama, Y., Flemming Hansen, D., Kay, L. E., *et al.* (2024) Mapping the FF domain folding pathway via structures of transiently populated folding intermediates. *Proc. Natl. Acad. Sci. U.S.A.* **121**, e2416682121
9. Tugarinov, V., and Clore, G. M. (2019) Exchange saturation transfer and associated NMR techniques for studies of protein interactions involving high-molecular-weight systems. *J. Biomol. NMR* **73**, 461–469
10. Zhuravleva, A., and Korzhnev, D. M. (2017) Protein folding by NMR. *Prog. Nucl. Magn. Reson. Spectrosc.* **100**, 52–77
11. Palmer, A. G., 3rd, and Koss, H. (2019) Chemical exchange. *Methods Enzymol.* **615**, 177–236
12. Vallurupalli, P., Sekhar, A., Yuwen, T., and Kay, L. E. (2017) Probing conformational dynamics in biomolecules via chemical exchange saturation transfer: a primer. *J. Biomol. NMR* **67**, 243–271
13. Torchia, D. A. (2011) Dynamics of biomolecules from picoseconds to seconds at atomic resolution. *J. Magn. Reson.* **212**, 1–10
14. Cavanagh, J., Fairbrother, W. J., Palmer, A. G., Rance, M., and Skelton, N. J. (2006) *Protein NMR Spectroscopy, Principles and Practice*, 2nd ed., Academic Press
15. Palmer, A. G., 3rd, Kroenke, C. D., and Loria, J. P. (2001) Nuclear magnetic resonance methods for quantifying microsecond-to-millisecond motions in biological macromolecules. *Methods Enzymol.* **339**, 204–238
16. Skrynnikov, N. R., Mulder, F. A., Hon, B., Dahlquist, F. W., and Kay, L. E. (2001) Probing slow time scale dynamics at methyl-containing side chains in proteins by relaxation dispersion NMR measurements: application to methionine residues in a cavity mutant of T4 lysozyme. *J. Am. Chem. Soc.* **123**, 4556–4566
17. Gopalan, A. B., Hansen, D. F., and Vallurupalli, P. (2018) CPMG experiments for protein minor conformer structure determination. *Methods Mol. Biol.* **1688**, 223–242
18. Palmer, A. G., and Massi, F. (2006) Characterization of the dynamics of biomacromolecules using rotating-frame spin relaxation NMR spectroscopy. *Chem. Rev.* **106**, 1700–1719
19. Rangadurai, A., Szymaski, E. S., Kimsey, I. J., Shi, H., and Al-Hashimi, H. (2019) Characterizing micro-to-millisecond chemical exchange in nucleic acids using off-resonance R1ρ relaxation dispersion. *Prog. Nucl. Magn. Reson. Spectrosc.* **112-113**, 55–102
20. Vallurupalli, P., Bouvignies, G., and Kay, L. E. (2012) Studying "invisible" excited protein states in slow exchange with a major state conformation. *J. Am. Chem. Soc.* **134**, 8148–8161

21. Ward, K. M., Aletras, A. H., and Balaban, R. S. (2000) A new class of contrast agents for MRI based on proton chemical exchange dependent saturation transfer (CEST). *J. Magn. Reson.* **143**, 79–87
22. Forsen, S., and Hoffman, R. A. (1963) Study of moderately rapid chemical exchange reactions by means of nuclear magnetic double resonance. *J. Chem. Phys.* **39**, 2892–2901
23. Milojevic, J., Esposito, V., Das, R., and Melacini, G. (2007) Understanding the molecular basis for the inhibition of the Alzheimer's Aβ-peptide oligomerization by human serum albumin using saturation transfer difference and off-resonance relaxation NMR spectroscopy. *J. Am. Chem. Soc.* **129**, 4282–4290
24. Fawzi, N. L., Ying, J., Ghirlando, R., Torchia, D. A., and Clore, G. M. (2011) Atomic-resolution dynamics on the surface of amyloid-beta protofibrils probed by solution NMR. *Nature* **480**, 268–272
25. Allerhand, A., and Thiele, E. (1966) Analysis of carr—purcell spin-echo NMR experiments on multiple-spin systems. II. The effect of chemical exchange. *J. Chem. Phys.* **45**, 902–916
26. Yuwen, T., Brady, J. P., and Kay, L. E. (2018) Probing conformational exchange in weakly interacting, slowly exchanging protein systems via off-resonance R1rho experiments: application to studies of protein phase separation. *J. Am. Chem. Soc.* **140**, 2115–2126
27. Sekhar, A., Rumfeldt, J. A. O., Broom, H. R., Doyle, C. M., Bouvignies, G., Meiering, E. M., *et al.* (2015) Thermal fluctuations of immature SOD1 lead to separate folding and misfolding pathways. *Elife* **4**, e07296
28. Deshmukh, L., Tugarinov, V., Appella, D. H., and Clore, G. M. (2018) Targeting a dark excited state of HIV-1 nucleocapsid by antiretroviral thioesters revealed by NMR spectroscopy. *Angew. Chem. Int. Ed. Engl.* **57**, 2687–2691
29. Lim, J., Xiao, T. S., Fan, J. S., and Yang, D. W. (2014) An off-pathway folding intermediate of an acyl carrier protein domain coexists with the folded and unfolded states under native conditions. *Angew. Chem. Int. Ed. Engl.* **53**, 2358–2361
30. Machado, L., De Paula, V. S., Pustovalova, Y., Bezsonova, I., Valente, A. P., Korzhnev, D. M., *et al.* (2018) Conformational dynamics of a cysteine-stabilized plant defensin reveals an evolutionary mechanism to expose hydrophobic residues. *Biochemistry* **57**, 5797–5806
31. Ahmed, R., Akcan, M., Khondker, A., Rheinstadter, M. C., Bozelli, J. C., Epand, R. M., *et al.* (2019) Atomic resolution map of the soluble amyloid beta assembly toxic surfaces. *Chem. Sci.* **10**, 6072–6082
32. Vallurupalli, P., and Kay, L. E. (2006) Complementarity of ensemble and single-molecule measures of protein motion: a relaxation dispersion NMR study of an enzyme complex. *Proc. Natl. Acad. Sci. U.S.A.* **103**, 11910–11915
33. Zhao, B., Hansen, A. L., and Zhang, Q. (2014) Characterizing slow chemical exchange in nucleic acids by carbon CEST and low spin-lock field $R_{1\rho}$ NMR spectroscopy. *J. Am. Chem. Soc.* **136**, 20–23
34. Ramanujam, V., Charlier, C., and Bax, A. (2019) Observation and kinetic characterization of transient schiff base intermediates by CEST NMR spectroscopy. *Angew. Chem. Int. Ed. Engl.* **58**, 15309–15312
35. Baase, W. A., Liu, L., Tronrud, D. E., and Matthews, B. W. (2010) Lessons from the lysozyme of phage T4. *Protein Sci.* **19**, 631–641
36. Mulder, F. A., Mittermaier, A., Hon, B., Dahlquist, F. W., and Kay, L. E. (2001) Studying excited states of proteins by NMR spectroscopy. *Nat. Struct. Biol.* **8**, 932–935
37. Feher, V. A., Baldwin, E. P., and Dahlquist, F. W. (1996) Access of ligands to cavities within the core of a protein is rapid. *Nat. Struct. Biol.* **3**, 516–521
38. Bouvignies, G., Vallurupalli, P., Hansen, D. F., Correia, B. E., Lange, O., Bah, A., *et al.* (2011) Solution structure of a minor and transiently formed state of a T4 lysozyme mutant. *Nature* **477**, 111–114
39. Lerch, M. T., Lopez, C. J., Yang, Z., Kreitman, M. J., Horwitz, J., and Hubbell, W. L. (2015) Structure-relaxation mechanism for the response of T4 lysozyme cavity mutants to hydrostatic pressure. *Proc. Natl. Acad. Sci. U.S.A.* **112**, E2437–E2446
40. Xue, M., Wakamoto, T., Kejlberg, C., Yoshimura, Y., Nielsen, T. A., Risor, M. W., *et al.* (2019) How internal cavities destabilize a protein. *Proc. Natl. Acad. Sci. U.S.A.* **116**, 21031–21036
41. Eriksson, A. E., Baase, W. A., Wozniak, J. A., and Matthews, B. W. (1992) A cavity-containing mutant of T4 lysozyme is stabilized by buried benzene. *Nature* **355**, 371–373
42. Mondal, J., Ahalawat, N., Pandit, S., Kay, L. E., and Vallurupalli, P. (2018) Atomic resolution mechanism of ligand binding to a solvent inaccessible cavity in T4 lysozyme. *PLoS Comput. Biol.* **14**, e1006180
43. Feher, V. A., Schiffer, J. M., Mermelstein, D. J., Mih, N., Pierce, L. C. T., McCammon, J. A., *et al.* (2019) Mechanisms for benzene dissociation through the excited state of T4 lysozyme L99A mutant. *Biophys. J.* **116**, 205–214
44. Nunes-Alves, A., Kokh, D. B., and Wade, R. C. (2021) Ligand unbinding mechanisms and kinetics for T4 lysozyme mutants from tauRAMD simulations. *Curr. Res. Struct. Biol.* **3**, 106–111
45. Schiffer, J. M., Feher, V. A., Malmstrom, R. D., Sida, R., and Amaro, R. E. (2016) Capturing invisible motions in the transition from ground to rare excited states of T4 lysozyme L99A. *Biophys. J.* **111**, 1631–1640
46. Vallurupalli, P., Chakrabarti, N., Pomes, R., and Kay, L. E. (2016) Atomistic picture of conformational exchange in a T4 lysozyme cavity mutant: an experiment-guided molecular dynamics study. *Chem. Sci.* **7**, 3602–3613
47. Brotzakis, Z. F., and Parrinello, M. (2019) Enhanced sampling of protein conformational transitions via dynamically optimized collective variables. *J. Chem. Theor. Comput* **15**, 1393–1398
48. Gopalan, A. B., Yuwen, T., Kay, L. E., and Vallurupalli, P. (2018) A methyl (1)H double quantum CPMG experiment to study protein conformational exchange. *J. Biomol. NMR* **72**, 79–91
49. Gopalan, A. B., and Vallurupalli, P. (2018) Measuring the signs of the methyl ^{1}H chemical shift diferences between major and 'invisible' minor protein conformational states using methyl ^{1}H multi-quantum spectroscopy. *J. Biomol. NMR* **70**, 187–202
50. Lundstrom, P., Vallurupalli, P., Religa, T. L., Dahlquist, F. W., and Kay, L. E. (2007) A single-quantum methyl 13C-relaxation dispersion experiment with improved sensitivity. *J. Biomol. NMR* **38**, 79–88
51. Vallurupalli, P., Hansen, D. F., Lundstrom, P., and Kay, L. E. (2009) CPMG relaxation dispersion NMR experiments measuring glycine 1H alpha and 13C alpha chemical shifts in the 'invisible' excited states of proteins. *J. Biomol. NMR* **45**, 45–55
52. Yuwen, T., and Kay, L. E. (2019) Revisiting (1)H(N) CPMG relaxation dispersion experiments: a simple modification can eliminate large artifacts. *J. Biomol. NMR* **73**, 641–650
53. Mulder, F. A., Skrynnikov, N. R., Hon, B., Dahlquist, F. W., and Kay, L. E. (2001) Measurement of slow (micros-ms) time scale dynamics in protein side chains by (15)N relaxation dispersion NMR spectroscopy: application to Asn and Gln residues in a cavity mutant of T4 lysozyme. *J. Am. Chem. Soc.* **123**, 967–975
54. Mulder, F. A., Hon, B., Mittermaier, A., Dahlquist, F. W., and Kay, L. E. (2002) Slow internal dynamics in proteins: application of NMR relaxation dispersion spectroscopy to methyl groups in a cavity mutant of T4 lysozyme. *J. Am. Chem. Soc.* **124**, 1443–1451
55. Rangadurai, A., Shi, H., and Al-Hashimi, H. M. (2020) Extending the sensitivity of CEST NMR spectroscopy to micro-to-millisecond dynamics in nucleic acids using high-power radio-frequency fields. *Angew. Chem. Int. Ed. Engl.* **59**, 11262–11266
56. Khandave, N. P., Sekhar, A., and Vallurupalli, P. (2023) Studying micro to millisecond protein dynamics using simple amide (15)N CEST experiments supplemented with major-state R(2) and visible peak-position constraints. *J. Biomol. NMR* **77**, 165–181
57. Khandave, N. P., Hansen, D. F., and Vallurupalli, P. (2024) Increasing the accuracy of exchange parameters reporting on slow dynamics by performing CEST experiments with 'high' B(1) fields. *J. Magn. Reson.* **363**, 107699
58. Sekhar, A., and Kay, L. E. (2013) NMR paves the way for atomic level descriptions of sparsely populated, transiently formed biomolecular conformers. *Proc. Natl. Acad. Sci. U.S.A.* **110**, 12867–12874
59. Tiwari, V. P., De, D., Thapliyal, N., Kay, L. E., and Vallurupalli, P. (2024) Beyond slow two-state protein conformational exchange using CEST: applications to three-state protein interconversion on the millisecond timescale. *J. Biomol. NMR* **78**, 39–60
60. Korzhnev, D. M., Salvatella, X., Vendruscolo, M., Di Nardo, A. A., Davidson, A. R., Dobson, C. M., *et al.* (2004) Low-populated folding

intermediates of Fyn SH3 characterized by relaxation dispersion NMR. *Nature* **430**, 586–590
61. Gladkova, C., Schubert, A. F., Wagstaff, J. L., Pruneda, J. N., Freund, S. M. V., and Komander, D. (2017) An invisible ubiquitin conformation is required for efficient phosphorylation by PINK1. *EMBO J.* **36**, 3555–3572
62. Vallurupalli, P., and Kay, L. E. (2013) Probing slow chemical exchange at carbonyl sites in proteins by chemical exchange saturation transfer NMR spectroscopy. *Angew. Chem. Int. Ed. Engl.* **52**, 4156–4159
63. Luo, Y., and Baldwin, R. L. (1998) Trifluoroethanol stabilizes the pH 4 folding intermediate of sperm whale apomyoglobin. *J. Mol. Biol.* **279**, 49–57
64. Korzhnev, D. M., Religa, T. L., Lundstrom, P., Fersht, A. R., and Kay, L. E. (2007) The folding pathway of an FF domain: characterization of an on-pathway intermediate state under folding conditions by (15)N, (13)C(alpha) and (13)C-methyl relaxation dispersion and (1)H/(2)H-exchange NMR spectroscopy. *J. Mol. Biol.* **372**, 497–512
65. Myers, J. K., Pace, C. N., and Scholtz, J. M. (1995) Denaturant m values and heat capacity changes: relation to changes in accessible surface areas of protein unfolding. *Protein Sci.* **4**, 2138–2148
66. Korzhnev, D. M., Religa, T. L., Banachewicz, W., Fersht, A. R., and Kay, L. E. (2010) A transient and low-populated protein-folding intermediate at atomic resolution. *Science* **329**, 1312–1316
67. Hansen, D. F., Vallurupalli, P., and Kay, L. E. (2008) Using relaxation dispersion NMR spectroscopy to determine structures of excited, invisible protein states. *J. Biomol. NMR* **41**, 113–120
68. Neudecker, P., Zarrine-Afsar, A., Davidson, A. R., and Kay, L. E. (2007) Phi-value analysis of a three-state protein folding pathway by NMR relaxation dispersion spectroscopy. *Proc. Natl. Acad. Sci. U.S.A.* **104**, 15717–15722
69. Korzhnev, D. M., Vernon, R. M., Religa, T. L., Hansen, A. L., Baker, D., Fersht, A. R., *et al.* (2011) Nonnative interactions in the FF domain folding pathway from an atomic resolution structure of a sparsely populated intermediate: an NMR relaxation dispersion study. *J. Am. Chem. Soc.* **133**, 10974–10982
70. Goto, N. K., Gardner, K. H., Mueller, G. A., Willis, R. C., and Kay, L. E. (1999) A robust and cost-effective method for the production of Val, Leu, Ile (delta 1) methyl-protonated 15N-, 13C-, 2H-labeled proteins. *J. Biomol. NMR* **13**, 369–374
71. Bouvignies, G., Vallurupalli, P., and Kay, L. E. (2014) Visualizing side chains of invisible protein conformers by solution NMR. *J. Mol. Biol.* **426**, 763–774
72. Bouvignies, G., and Kay, L. E. (2012) A 2D C-13-CEST experiment for studying slowly exchanging protein systems using methyl probes: an application to protein folding. *J. Biomol. NMR* **53**, 303–310
73. Guenneugues, M., Berthault, P., and Desvaux, H. (1999) A method for determining B_1 field inhomogeneity. Are the biases assumed in heteronuclear relaxation experiments usually underestimated? *J. Magn. Reson.* **136**, 118–126
74. McConnell, H. M. (1958) Reaction rates by nuclear magnetic resonance. *J. Chem. Phys.* **28**, 430–431
75. Hansen, D. F., Vallurupalli, P., and Kay, L. E. (2008) An improved 15N relaxation dispersion experiment for the measurement of millisecond time-scale dynamics in proteins. *J. Phys. Chem. B* **112**, 5898–5904
76. Vallurupalli, P., Scott, L., Williamson, J. R., and Kay, L. E. (2007) Strong coupling effects during X-pulse CPMG experiments recorded on heteronuclear ABX spin systems: artifacts and a simple solution. *J. Biomol. NMR* **38**, 41–46
77. Delaglio, F., Grzesiek, S., Vuister, G. W., Zhu, G., Pfeifer, J., and Bax, A. (1995) NMRPipe - a multidimensional spectral processing system based on unix pipes. *J. Biomol. NMR* **6**, 277–293
78. Goddard, T. D., and Kneller, D. G. (2008) *SPARKY 3 University of California, San Francisco*
79. Lee, W., Tonelli, M., and Markley, J. L. (2015) NMRFAM-SPARKY: enhanced software for biomolecular NMR spectroscopy. *Bioinformatics* **31**, 1325–1327
80. Ahlner, A., Carlsson, M., Jonsson, B. H., and Lundstrom, P. (2013) PINT: a software for integration of peak volumes and extraction of relaxation rates. *J. Biomol. NMR* **56**, 191–202
81. Press, W. H., Flannery, B. P., Teukolsky, S. A., and Vetterling, W. T. (1992) *Numerical Recipes in C. the Art of Scientific Computing*, Second Edition, Cambridge University Press, Cambridge (UK)
82. Choy, W. Y., Zhou, Z., Bai, Y., and Kay, L. E. (2005) An 15N NMR spin relaxation dispersion study of the folding of a pair of engineered mutants of apocytochrome b562. *J. Am. Chem. Soc.* **127**, 5066–5072
83. Liu, L. J., Baase, W. A., and Matthews, B. W. (2009) Halogenated benzenes bound within a non-polar cavity in T4 lysozyme provide examples of I—S and I–Se halogen-bonding. *J. Mol. Biol.* **385**, 595–605
84. Skrynnikov, N. R., Dahlquist, F. W., and Kay, L. E. (2002) Reconstructing NMR spectra of "invisible" excited protein states using HSQC and HMQC experiments. *J. Am. Chem. Soc.* **124**, 12352–12360